2021

High-Tide Floods and Storm Surges During Atmospheric Rivers on the US West Coast

Christopher G. Piecuch

Sloan Coats

Sönke Dangendorf
Old Dominion University, sdangend@odu.edu

Felix W. Landerer

J. T. Reager

See next page for additional authors

Authors

Christopher G. Piecuch, Sloan Coats, Sönke Dangendorf, Felix W. Landerer, J. T. Reager, Philip R. Thompson, and Thomas Wahl

Coversheet for "High-Tide Floods and Storm Surges During Atmospheric Rivers on the US West Coast'

3 Christopher G. Piecuch[1,†], Sloan Coats[2], Sönke Dangendorf[3], Felix W. Landerer[4], J. T. Reager[4],

4 Philip R. Thompson[2], and Thomas Wahl[5]

5 [1] *Woods Hole Oceanographic Institution, Woods Hole, Massachusetts, USA*

6 [2] *University of Hawai'i at Mānoa, Honolulu, HI, USA*

7 [3] *Old Dominion University, Norfolk, VA, USA*

8 [4] *Jet Propulsion Laboratory, Pasadena, CA, USA*

9 [5] *University of Central Florida, Orlando, FL, USA*

13 † cpiecuch@whoi.edu

1

[1] High-Tide Floods and Storm Surges During
[2] Atmospheric Rivers on the US West Coast

Christopher G. Piecuch[1], Sloan Coats[2], Sönke Dangendorf[3], Felix W.

Landerer[4], J. T. Reager[4], Philip R. Thompson[2], and Thomas Wahl[5]

———

Christopher G. Piecuch, Woods Hole Oceanographic Institution, 266 Woods Hole Road, Woods

Hole, MA 02543, USA. (cpiecuch@whoi.edu)

[1]Woods Hole Oceanographic Institution,

Woods Hole, MA, USA.

[2]University of Hawai'i at Mānoa,

Honolulu, HI, USA.

[3]Old Dominion University, Norfolk, VA,

USA

[4]Jet Propulsion Laboratory, Pasadena,

CA, USA.

[5]University of Central Florida, Orlando,

FL, USA.

D R A F T   August 24, 2021, 2:20pm   D R A F T

Abstract. Atmospheric rivers (ARs) effect inland hydrological impacts

related to extreme precipitation. However, little is known about the

possible coastal hazards associated with these storms. Here we elucidate

high-tide floods (HTFs) and storm surges during ARs through a

statistical analysis of data from the US West Coast during 1980–2016.

HTFs and landfalling ARs co-occur more often than expected from

random chance. Between 10%–63% of HTFs coincide with landfalling

ARs, depending on location. However, only 2%–15% of ARs coincide with

HTFs, suggesting that ARs typically must co-occur with anomalously

high tides or mean sea levels to cause HTFs. Storm surges during ARs

are interpretable in terms of local wind, pressure, and precipitation

forcing. Meridional wind and barometric pressure are the primary drivers

of the storm surge. This study highlights the relevance of ARs to coastal

impacts, clarifies the drivers of storm surge during ARs, and identifies

future research directions.

18   **Plain Language Summary.** ARs drive hydrological hazards over land

19 related to extreme precipitation. As they make landfall, ARs bring heavy

20 rains, strong winds, and low pressures to the coast. While these factors

21 can cause storm surge and coastal flooding, little attention has been paid

22 to possible coastal impacts of ARs. We establish relationships between

23 ARs and HTFs on the US West Coast and identify the factors causing

24 storm surge during ARs. HTFs occur at nearly the same time that ARs

25 make landfall more often than expected from random chance. This means

26 that ARs contribute importantly to HTFs. Even so, few ARs lead to

27 HTFs—favorable tides or mean sea-level anomalies are usually needed on

28 top of the storm surge from an AR to cause a HTF. Storm surge during

29 an AR can be explained by the heavy rain, strong wind, and low pressure

30 associated with the storm. Wind and pressure are the primary factors

31 causing the surge during an AR event. Our results highlight how HTFs

32 arise from the subtle interweaving of storm surge, tide, and mean

33 sea-level effects, thus providing important information to coastal

34 managers and ocean modelers, and motivating future studies to more

35 comprehensively investigate relationships between ARs and coastal

36 hazards globally.

Key Points:

- HTFs on the US West Coast co-occur with landfalling ARs more often than expected from random chance.

- Between 10%–63% of HTFs observed by tide gauges coincide with landfalling ARs, depending on location.

- Meridional wind and barometric pressure make the main contributions to storm surge during landfalling ARs.

1. Introduction

Atmospheric rivers (ARs) are long, narrow filaments of strong horizontal water vapor transport in the lower troposphere, typically associated with cold fronts of extratropical cyclones (Cordeira et al., 2013; Ralph et al., 2004; Ralph et al., 2017). ARs play an important role in the hydrological cycle, accomplishing most of the poleward moisture transport in the atmosphere at midlatitudes (Newman et al., 2012; Zhu and Newell, 1998). Landfalling ARs can be forced upwards by orography, leading to extreme precipitation and a range of hydrological impacts (Neiman et al., 2008). In California, for example, precipitation due to ARs has ended droughts and caused floods, landslides, and other debris flows (Dettinger, 2013; Du et al., 2018; Hendy et al., 2015; Oakley et al., 2017; Oakley et al., 2018; Ralph et al., 2013; Wang et al., 2017; White et al., 2019).

While most studies of hazards related to ARs focus on hydrological impacts (Payne et al., 2020), the conditions typifying ARs—heavy rain, strong wind, low pressure—also drive storm surge at the coast (Gill, 1982; Pugh and Woodworth, 2014). This suggests

D R A F T   August 24, 2021, 2:20pm   D R A F T

57 that ARs could be relevant to coastal impacts, such as high-tide floods (HTFs;

58 Moftakhari et al., 2018; Sweet and Park, 2014; Sweet et al., 2021), which negatively

59 affect transportation, property, and public health and safety (Hino et al., 2019;

60 Moftakhari et al., 2017). The frequency of HTFs along the US West Coast has increased

61 in recent decades in some places (San Diego, La Jolla, San Francisco, and Seattle), and

62 more generally shows interannual variability that correlates with phases of the El

63 Niño-Southern Oscillation (ENSO; Sweet et al., 2021). However, few studies investigate

64 the relationship between coastal sea level and ARs.

65   Khouakhi and Villarini (2016) quantify the correspondence between ARs and extreme

66 sea-level statistics on the US West Coast. They find that annual maxima of hourly still

67 water levels at tide gauges between San Diego, California and Tofino, British Columbia

68 occur within 12 hours of passing ARs 15–50% of the time. These authors also determine

69 a relationship with modes of large-scale climate variability. For example, exceedances

70 over the 99.5th percentile of the hourly still water level distribution during ARs occur

71 more frequently during El Niños and less frequently during La Niñas.

72   Shinoda et al. (2019) study the oceanic response to ARs during the CalWater 2015

73 field campaign. They observe daily averaged still water level anomalies of 30–50 cm at

74 the Neah Bay, Washington and South Beach, Oregon tide gauges coinciding with

75 landfalling ARs on 16th January and 6th February 2015. These authors determine that

76 a high-resolution ocean general circulation model reproduces the timing of observed

77 storm surges, but only about half of their magnitude. Shinoda et al. (2019) posit that

78   the storm-surge response is mainly due to alongshore winds and coastal currents, and

79   that model-data discrepancies reflect small-scale processes unresolved by the model.

80   These studies advance understanding of ARs and their impacts on sea level, but they

81   also imply outstanding questions. First, the relationship between ARs and coastal

82   impacts remains unclear. For instance, annual-maxima and peaks-over-threshold

83   statistics from Khouakhi and Villarini (2016) are not necessarily informative of HTFs.

84   Annual maxima do not correspond to HTFs in years without HTFs, and this statistic

85   overlooks HTFs during years with multiple HTFs. Likewise, the 99.5th percentile of a

86   still water level distribution usually does not correspond to, and tends to be lower than,

87   impact thresholds (Table S1; Sweet et al., 2018), meaning that many peaks over

88   thresholds studied by Khouakhi and Villarini (2016) do not correspond to HTFs.

89   Second, the factors driving storm surge during ARs remain to be established. For

90   example, Shinoda et al. (2019) interpret storm surges during ARs in terms of the

91   ocean's dynamic response to wind forcing. Their interpretation contrasts with Bromirski

92   et al. (2017), who reason that the ocean's isostatic adjustment to barometric pressure is

93   the primary mechanism of storm surge along the US West Coast. Khouakhi and

94   Villarini (2016) recommend a future study to clarify the roles of wind and pressure

95   forcing on storm surges during ARs.

96   Here we address these outstanding questions related to ARs, HTFs, and storm surges

97   on the US West Coast. We consider tide-gauge data, HTF thresholds, a catalog of ARs,

98   and a gridded atmospheric reanalysis to establish the relationship between ARs and

99   HTFs as well as the factors forcing storm surge during ARs. Results reveal that ARs

100   contribute significantly to HTFs on the US West Coast, and clarify the relative effects of

101   wind, pressure, and precipitation forcing on the associated storm surges.

2. Data

102   We use hourly still water level observations, tidal predictions, and station datums for

103   24 tide gauges on the US West Coast from the National Oceanic and Atmospheric

104   Administration (NOAA) Center for Operational Oceanographic Products and Services

105   (CO-OPS). These records are selected because they are relatively long, complete, and

106   span much of the US West Coast (Figure S1; Table S1). They also represent the union of

107   US stations considered either in past studies of ARs and sea level on the US West Coast

108   (Khouakhi and Villarini, 2016; Shinoda et al., 2019) or in government reports on HTFs

109   (e.g., Sweet et al., 2021), allowing us to interpret our results in light of past findings.

110   We also use the Scripps Institution of Oceanography AR catalog of Gershunov et al.

111   (2017), which is generated by applying an automated AR detection algorithm to

112   6-hourly integrated water vapor transport (IVT) and integrated water vapor (IWV)

113   from the National Centers for Environmental Prediction/National Center for

114   Atmospheric Research (NCEP/NCAR) Reanalysis 1 (Kalnay et al., 1996). Landfalling

115   ARs are identified by their spatial extent ($\geq$ 1500 km), temporal duration ($\geq$ 18 hours),

116   IVT ($\geq$ 250 kg m^{-1} s^{-1}), and IWV ($\geq$ 15 mm). The landfalling location of an AR

117   satisfying these criteria is defined as the reanalysis grid cell with the maximum IVT

118   along the coast. The catalog includes the time, location, IWT, IVT, and zonal and

119   meridional wind of ARs at their landfalling locations on a 2.5° $\times$ 2.5° grid along the US

120   West Coast (22.5–57.5°N, 105–135°W; Figure S1) from January 1948 to March 2017. To

121 complement information provided by the Gershunov et al. (2017) catalog, we also

122 consider daily meridional and zonal wind stress, barometric pressure, and precipitation

123 from the NCEP/NCAR Reanalysis 1.

124   We consider the data between 1 January 1980 and 31 December 2016. The start date

125 is chosen partly based on the tide-gauge records, many of which begin in the late 1970s.

126 By not considering data prior to 1980, we also avoid possible discontinuities in the

127 reanalysis related to the advent of satellite data in the late 1970s. Data processing and

128 methods specific to the analysis of either HTFs or storm surges are described in the next

129 two sections before the respective results are introduced.

3. High-tide floods

130   We establish relationships between ARs and HTFs on the US West Coast using a

131 peaks-over-threshold approach (cf. Khouakhi and Villarini, 2016). For each tide gauge,

132 we count the number of days when HTFs occur for at least one hour (HTF days). We

133 identify HTFs when still water levels exceed the local minor flood thresholds defined by

134 Sweet et al. (2018), which range between 56–64 cm above local mean higher high water

135 (Table S1). We also count the number of days when an AR passes nearby a tide gauge

136 (AR days). An AR is nearby a tide gauge when it has IVT ≥ 500 kg m^{-1} s^{-1} and is in

137 the grid cell whose centroid is closest to the gauge (Figure S1). Note that results are

138 qualitatively insensitive to reasonable alternative definitions of "nearby" (Figure 2a).

139 We also count the number of days when both a HTF occurs and an AR passes nearby

140 the gauge within 24 hours of the HTF (HTF-and-AR days). Finally, we count the

141 hypothetical number of days when HTFs would have occurred from mean sea-level

D R A F T   August 24, 2021, 2:20pm   D R A F T

142   changes and tides alone, absent any surges, by removing the predicted tide from the

143   hourly water level data, low-pass filtering the non-tidal residuals with a 20-day moving

144   median operator, adding back the predicted tide, and identifying days when the flood

145   threshold is exceeded. We run 1,000 bootstrap iterations to estimate uncertainty due to

146   the finite record length of the data (Supporting Information Text S1). We quantify

147   statistical significance by comparing observed values to values determined synthetically

148   through 1,000 simulations of stochastic processes (Supporting Information Text S2).

149   HTF days and AR days along the US West Coast show clear spatial structure

150   (Figures 1a, 1b). More HTF days and AR days were experienced on the Northwest

151   Coast than the Southwest Coast. For example, San Diego, California experienced

152   79 ± 17 HTF days and 259 ± 30 AR days during the study period, whereas Neah Bay,

153   Washington witnessed 329 ± 37 HTF days and 760 ± 54 AR days over that same time.

154   All $\pm$ ranges identify 95% confidence intervals based on bootstrapping. The Puget

155   Sound is an exception to the rule: fewer HTF days and AR days occurred at

156   higher-latitude tide gauges in this estuary compared to lower-latitude tide gauges on the

157   open-ocean coasts of Oregon and Washington, suggesting that these estuarine locations

158   are more sheltered from processes driving HTFs and ARs. Central California also

159   deviates from the trend, as fewer HTF days were observed at mid-latitude locations in

160   this region compared to lower-latitude sites in Southern California. The basic patterns

161   of HTF days and AR days found here are consistent with previous studies. For example,

162   Sweet et al. (2021) report that more HTFs happen on the open coasts of Oregon and

163   Washington than on the California coast or within the Puget Sound (their Appendix 1),

D R A F T   August 24, 2021, 2:20pm   D R A F T

164 while Neiman et al. (2008) find that more AR days occur on the Northwest Coast of

165 North America than on the Southwest Coast. However, past studies do not interrogate

166 possible connections between HTFs and ARs.

167   To clarify relationships between ARs and HTFs, we compute percentages of HTF

168 days that are AR days and AR days that are HTF days (Figures 1c, 1d, 2a). The

169 percentage of HTF days that are AR days quantifies whether ARs are a necessary

170 condition for HTFs (values $\sim 100\%$ indicate that HTFs only occur during ARs), while

171 the percentage of AR days that are HTF days measures whether ARs are a sufficient

172 condition for HTFs (values $\sim 100\%$ indicate that ARs always lead to HTFs). On

173 average along the coast, $28\% \pm 2.3\%$ of HTF days are AR days, but values are elevated

174 between Monterey and Arena Cove ($48\% \pm 6.9\%$) in Central California, with the highest

175 percentage ($63\% \pm 19\%$) observed at San Francisco (Figures 1c, 3a). In comparison, the

176 percentage of AR days that are HTF days is lower on average ($5.2\% \pm 0.4\%$), peaking

177 more to the north, with $10\% \pm 1.1\%$ of AR days being HTF days between Port Orford,

178 Oregon and Toke Point, Washington (Figure 1d), suggesting that ARs alone are seldom

179 sufficient to cause HTFs. Nevertheless, at nearly all sites, values in Figures 1c, 1d, 2a

180 are statistically significant ($P < 0.05$), meaning that HTFs and ARs co-occur more often

181 than expected from random chance, and that ARs are important contributors to HTFs.

182   HTF and AR frequencies also vary across time (Figure 2b). The annual number of

183 HTFs averaged along the US West Coast varies from 0.7 ± 0.7 to 13 ± 5.9 days per year,

184 while the average number of ARs ranges between 7.2 ± 3.1 and 21 ± 6.3 days per year

185 (Figure 2b). HTF days were highest in 1982 (13 ± 5.9 days) and 1997 (12 ± 5.4 days)

186 during strong positive ENSO events. This observation is consistent with past studies

187 identifying a relationship between ENSO and HTF frequency on the US West Coast

188 (Sweet and Park, 2014; Sweet et al., 2021). The Pearson correlation coefficient between

189 interannual variations in HTF and AR days on the US West Coast (0.2 ± 0.2) is not

190 statistically significant ($P > 0.05$). In contrast, the number of HTF days per year is

191 significantly correlated with annual mean sea-level anomaly averaged along the coast

192 (0.7 ± 0.1, $P < 0.01$; Figure 2b). An even higher correlation (0.9 ± 0.1, $P < 0.01$) is

193 found between observed HTF days and hypothetical HTF days expected from tides and

194 mean sea-level changes, such that the latter explains $66 \pm 14\%$ of the variance in the

195 former, suggesting that changes in these extreme sea-level events are governed more by

196 tides and mean sea-level changes than changes in storminess (cf. Marcos et al., 2015;

197 Menéndez and Woodworth, 2010; Ray and Merrifield, 2019; Thompson et al., 2021).

4. Storm surges

198 We quantify storm surges and their causes during ARs on the US West Coast using a

199 composite analysis (cf. Shinoda et al., 2019). We identify all ARs passing by tide gauges

200 during the study period. For each AR as it passes by a gauge, we isolate the time when

201 maximum IVT takes place and interpret it as when the gauge experiences the strongest

202 effect of the AR. We then take the associated daily storm surge from the tide gauge,

203 which we calculate from daily-mean still water level by removing the predicted tide,

204 seasonal cycle, and linear trend, and then applying a high-pass filter based on a 20-day

205 moving median operator.

206   Storm surges during ARs show clear spatial structure (Figures 3a, 3b, 4a). Surges are

207   larger on average at higher latitudes (Figures 3a, 4a). Mean storm surge during an AR

208   grows from 3.1 ± 1.2 cm at Santa Monica, California to 21 ± 3.2 cm at Toke Point,

209   Washington. Deviations from this trend are apparent at locations in the Puget Sound,

210   where mean surge values are lower than expected from latitude alone, which could

211   reflect important estuarine processes distinct from the mechanisms that mediate storm

212   surge along the open-ocean coastline. Storm surge is also more variable at higher

213   latitudes (Figure 3b). For example, the standard deviation of storm surge during ARs is

214   4.3 ± 0.8 cm at La Jolla, California, 12 ± 1.6 cm at South Beach, Oregon, and 20 ± 5.3

215   cm at Toke Point, Washington. [Note that, while we use mean and standard deviation

216   as summary statistics, storm surge distributions are not Gaussian (Figure S2).] Such

217   surges are rarely large enough, when superimposed on mean higher high water, to

218   overtop flood thresholds (cf. Table S1; Figure S2). This corroborates the suggestion

219   made in the previous section that ARs alone are seldom sufficient to cause HTFs.

220   These basic patterns are qualitatively consistent with previous numerical studies of

221   sea level and ARs as well as past observational studies of storm surge in the region.

222   Considering tide-gauge data during 1935–2014, Bromirski et al. (2017) show that the

223   99th percentile of hourly non-tidal winter residuals increases steadily from 10–15 cm in

224   Southern California to 45–55 cm in Oregon and Washington (their Figure 2c). Serafin et

225   al. (2017) reveal that the average and spread of observed annual maxima in hourly

226   non-tidal residuals from 11 tide gauges between La Jolla, California and Neah Bay,

227   Washington increase from south to north along the coast (their Figure 1e). Using a

228 high-resolution ocean general circulation model, Shinoda et al. (2019) report that

229 coastal sea level rises during the days leading up to an AR by between $\lesssim 1$ cm off

230 Southern California to $\gtrsim 4$ cm off Oregon and Washington (their Figure 8h). However,

231 these studies do not establish what processes drive storm surge during landfalling ARs.

To attribute observed surges (Figures 3a, 3b), we use contemporaneous daily zonal

and meridional wind stress, barometric pressure, and precipitation from NCEP/NCAR

Reanalysis 1 at the grid cells closest to the tide gauges. We remove seasonal cycles and

linear trends from the reanalysis and apply a 20-day high-pass filter. To quantify how

much storm surge can be understood in terms of local wind, pressure, and precipitation

anomalies, we consider a simple model that represents surge as a linear superposition of

the atmospheric forcing

$$\zeta = \overbrace{\underbrace{a_\pi \pi + b_\pi \mathcal{H}(\pi)}_{\hat{\zeta}_\pi} + \underbrace{a_\tau \tau + b_\tau \mathcal{H}(\tau)}_{\hat{\zeta}_\tau} + \underbrace{a_p p + b_p \mathcal{H}(p)}_{\hat{\zeta}_p} + \underbrace{a_q q + b_q \mathcal{H}(q)}_{\hat{\zeta}_q}}^{\hat{\zeta}} + \epsilon. \qquad (1)$$

232 Here ζ is storm surge, π and τ are zonal and meridional wind stress, respectively, p is

233 barometric pressure, q is precipitation, $\mathcal{H}$ is Hilbert transform, the a's and b's are real

234 constants, and ϵ is a residual. The Hilbert transform rotates each Fourier component of

235 a time series by $\pm 90°$ (Thomson and Emery, 2014). Thus, including Hilbert transforms

236 on the right-hand side of Eq. (1) allows for general phase relationships between the

237 atmospheric forcing and the oceanic response. For clarity, let $\hat{\zeta}_\pi$, $\hat{\zeta}_\tau$, $\hat{\zeta}_p$, and $\hat{\zeta}_q$ identify

238 the modeled ζ responses to π, τ, p, and q forcing, respectively, and $\hat{\zeta}$ the total modeled ζ

239 response. We use ridge regression to determine the a's and b's at each tide gauge

240 (Supporting Information Text S3), which is preferable to ordinary least squares given

241   possible collinearity between predictors. Results are based on a ridge-parameter value of

242    $\lambda = 0.3$, but similar findings follow from a range of λ values (Figure S3).

243   Modeled $\hat{\zeta}$ shows skill in explaining ζ observed at tide gauges (Figures 3, 4). The

244   model reproduces the observed structure that surges grow larger and more variable with

245   latitude along the coast (Figure 3). Mean storm surges from the observations ζ and the

246   model $\hat{\zeta}$ overlap within estimated uncertainties everywhere on the California coast

247   (Figure 4a). Along Oregon and Washington, the model can underestimate observed

248   mean storm surge (by as much as 32% on average at Cherry Point, Washington),

249   possibly due to shrinkage related to the ridge regression, reanalysis errors (e.g., due to

250   coarse grid cells that overlap land and sea), or processes absent from the model (Figure

251   4a). The model also accounts for most of the observed storm-surge variation at all

252   gauges (Figure 4b), explaining between $57 \pm 20\%$ (La Jolla, California) and $87 \pm 3.4\%$

253   (Point Reyes, California) of the variance in the data.

254   The model is also informative of the relative influences of π, τ, p, and q forcing on ζ

255   (Figure 4). Primary contributions to ζ are made by p and τ (Figure 4). On average, $\hat{\zeta}_p$

256   contributions to mean ζ values are nearly spatially uniform along the coast, ranging

257   between 2–5 cm (Figure 4a). In contrast, average $\hat{\zeta}_\tau$ values become larger with latitude,

258   growing from 0.3 ± 0.9 cm at Santa Monica, California to 11 ± 2.3 cm at Toke Point,

259   Washington. In Southern California and within Puget Sound, $\hat{\zeta}_p$ is the more important

260   contributor to ζ variance, but elsewhere $\hat{\zeta}_\tau$ and $\hat{\zeta}_p$ contribute comparably (Figure 4b).

261   Forcing by q can also make secondary contributions (Figure 4). Mean $\hat{\zeta}_q$ values are

262   distinguishable from zero at most sites, reaching as high as 2.3 ± 0.8 cm in Point Reyes,

D R A F T   August 24, 2021, 2:20pm   D R A F T

263 California and 3.2 ± 2.0 cm in Toke Point, Washington (Figure 4a). In and around San

264 Francisco Bay, and along portions of the Washington coast, $\hat{\zeta}_q$ explains 10–20% of the ζ

265 variance on average (Figure 4b). In contrast, π forcing is largely insignificant (Figure 4).

266 In most places, estimates of ζ variance explained by $\hat{\zeta}_\pi$ overlap with zero (Figure 4b),

267 and mean $\hat{\zeta}_\pi$ values are indistinguishable from zero or small and negative (Figure 4a).

5. Summary and Discussion

268 Atmospheric rivers (ARs) bring heavy rain, strong wind, and low pressure to the

269 coastal zone. We established relationships between ARs and high-tide floods (HTFs),

270 and identified forcing mechanisms responsible for storm surge during ARs on the US

271 West Coast during 1980–2016. ARs and HTFs co-occur more often than expected from

272 random chance, and 10–63% of HTFs coincide with ARs, depending on location (Figures

273 1, 2). Interannual variations in HTF days and AR days per year are not significantly

274 correlated (Figure 2), meaning that more ARs do not necessarily result in more HTFs.

275 Instead, there is a significant correlation between observed HTF days per year and the

276 HTF days expected from tides and mean sea-level changes alone (Figure 2). A linear

277 model including local wind, pressure, and precipitation forcing accounts for $\geq 68\%$ of the

278 average magnitude and 57–87% of the variance in magnitude of storm surges during ARs

279 (Figures 3, 4). Meridional wind and barometric pressure make primary contributions to

280 storm surge, but precipitation has a secondary effect in some places (Figure 4).

281 HTFs arise from a subtle interplay of distinct processes acting on different timescales.

282 Fewer HTFs would occur from tides and mean sea-level changes in the absence of surges

283 due to ARs and other storms (Figure 2), but surges associated with ARs are rarely large

284   enough, when added to mean higher high water, to cause HTFs on their own (Figure 3);

285   only when superimposed on a favorable tide or mean sea-level anomaly are storm surges

286   related to ARs generally capable of exceeding HTF thresholds. For a full understanding

287   of observed HTFs, the effects of surges, tides, and mean sea level must all be considered.

288   This paper advances knowledge of hazards related to ARs and the oceanic response to

289   atmospheric forcing on the US West Coast. Past studies emphasize hydrological impacts

290   of ARs related to extreme precipitation (Payne et al., 2020), but we show that ARs also

291   drive coastal impacts related to sea level. By quantifying relationships between HTFs

292   and ARs, and identifying the factors driving storm surge during these events, we resolve

293   outstanding questions in the literature (Bromirski et al., 2017; Khouakhi and Villarini,

294   2016; Shinoda et al., 2019). This paper elucidates a mechanism of HTFs, occurrences of

295   which are increasing on much of the US Coast (Sweet et al., 2021), and will accelerate

296   into the future (Thompson et al., 2021). Our work is consistent with the notion that

297   observed changes in sea-level extremes are attributable more to changes in mean sea

298   level and the tides than to changes in storminess (Marcos et al., 2015; Menéndez and

299   Woodworth, 2010; Ray and Merrifield, 2019; Thompson et al., 2021). Our results also

300   underscore the importance of understanding locally forced high-frequency sea-level

301   variability on the US West Coast (Battisti and Hickey, 1984; Bromirski et al., 2017;

302   Chapman, 1987; Gill and Clarke, 1974; Ryan and Noble, 2006; Verdy et al., 2014).

303   We conclude with some limitations of our study and future research directions.

304   1. Space constraints precluded a complete study of the spatiotemporal statistics of

305   HTFs and ARs on the US West Coast. Future studies should consider more granular

306   details, such as temporal variation in HTF and AR co-occurrences at individual tide

307   gauges across various timescales, including the seasonal cycle and decadal trends, to

308   identify whether sea-level rise influences the covariance between HTFs and ARs, and if

309   HTFs due to ARs occur mainly in particular months of the year (Thompson et al., 2021).

310   2. We focused on the US West Coast, but ARs make landfall in other mid- and

311   high-latitude regions (Payne et al., 2020). Links should be established between ARs and

312   sea-level extremes on a more global basis (cf. Ridder et al., 2018; Carvajal et al., 2021).

313   3. We used the catalog of Gershunov et al. (2017), but other AR catalogs are

314   available, which can differ in terms of their detection algorithms (Rutz et al., 2019;

315   Shields et al., 2018). Multiple catalogs should be considered to more thoroughly

316   quantify uncertainty.

317   4. We focused on storm surge and HTFs, but ARs could affect other quantities of

318   interest to coastal impacts, such as waves and erosion (Serafin et al., 2017; Theuerkauf et

319   al., 2014). A more comprehensive assessment of coastal hazards due to landfalling ARs,

320   including their role in compound events (AghaKouchak et al., 2020), should be made.

321   5. We used flood thresholds from the common impact threshold framework of Sweet

322   et al. (2018), which is a consistent national coastal flood metric, applicable everywhere

323   tidal datums are established. However, flood thresholds based on this framework may be

324   lower or higher than levels that correspond to local impacts (Kriebel and Geiman, 2013).

325   The sensitivity of our results to other definitions of flood threshold should be quantified.

326   6. Our investigation of storm surge was statistical in nature. Regression coefficients

327   found empirically from the data are consistent with basic expectations from ocean

328   dynamics (Supporting Information Text S4; Figure S3), suggesting that we identify

329   causal relationships between storm surge and atmospheric forcing. Even so, a more

330   physics-based assessment would be informative, allowing the relative roles of the various

331   (correlated) forcing mechanisms to be more unambiguously identified.

332   7. We used observations of the past four decades, but the nature of ARs could change

333   under future warming. While their dynamical response to climate change remains

334   uncertain (Shepherd et al., 2014; Vallis et al., 2015), ARs are expected to become more

335   frequent (Espinoza et al., 2018), contain more moisture (Dettinger, 2011), and shift

336   poleward (Yin, 2005) as the climate changes. It remains to evaluate how future changes

337   in ARs would aggravate coastal impacts already expected from future sea-level rise

338   (Jevrejeva et al., 2019; Kopp et al., 2017).

344   **Data Availability Statement.** Tide-gauge data, tidal predictions, and station

345   datum information were taken from the NOAA Tides and Currents Service

346   (`https://tidesandcurrents.noaa.gov/`); codes used for downloading the data are

347   available through Zenodo (`10.5281/zenodo.5247207`). Reanalysis fields are available

348   from the NOAA Physical Sciences Laboratory

349   (`https://psl.noaa.gov/data/gridded/data.ncep.reanalysis.html`). The AR data

350   were downloaded from the Scripps Institution of Oceanography

351   (`https://weclima.ucsd.edu/data-products/`).

References

352   AghaKouchak, A., Chiang, F., Huning, L. S., Love, C. A., Mallakpour, I., Mazdiyasni,

353   O., Moftakhari, H., Papalexiou, S. M., Ragno, E., & Sadegh, M. (2020). Climate

354   Extremes and Compound Hazards in a Warming World. *Annual Review of Earth and*

355   *Planetary Sciences*, *48*, 519–548.

356   Battisti, D. S., & Hickey, B. M. (1984). Application of Remote Wind-Forced Coastal

357   Trapped Wave Theory to the Oregon and Washington Coasts. *Journal of Physical*

358   *Oceanography*, *14*, 887–903.

359   Bromirski, P. D., Flick, R. E., & Miller, A. J. (2017). Storm surge along the Pacific coast

360   of North America. *Journal of Geophysical Research: Oceans*, *122*, 441–457.

361   Carvajal, M., Winckler, P., Garreaud, R., Igualt, F., Contreras-López, M., Averil, P.,

362   Cisternas, M., Gubler, A., & Breuer, W. A. (2021). Extreme sea levels at Rapa Nui

363   (Easter Island) during intense atmospheric rivers. *Natural Hazards*, *106*, 1619–1637.

364   Chapman, D. C. (1987). Application of Wind-Forced, Long, Coastal-Trapped Wave

365   Theory Along the California Coast. *Journal of Geophysical Research*, *92*, C2,

366   1798–1816.

367   Cordeira, J. M., Ralph, F. M., & Moore, B. J. (2013). The development and evolution of

368   two atmospheric rivers in proximity to western North Pacific tropical cyclones in

369   October 2010. *Monthly Weather Review*, *141*, 2434–4255.

Dettinger, M. D. (2013). Atmospheric rivers as drought busters on the US West Coast. *Journal of Hydrometeorology*, *14*, 1721–1732.

Dettinger, M. D. (2011). Climate change, atmospheric rivers, and floods in California—a multimodel analysis of storm frequency and magnitude changes. *Journal of the American Water Resources Association*, *14*, 514–523.

Du, X., Hendy, I., & Schimmelmann, A. (2018). A 9000-year flood history for Southern California: a revised stratigraphy of varved sediments in Santa Barbara Basin. *Marine Geology*, *397*, 29–42.

Espinoza, V., Waliser, D. E., Guan, B., Lavers, D. A., & Ralph, F. M. (2018). Global analysis of climate change projection effects on atmospheric rivers. *Geophysical Research Letters*, *45*, 4299–4308.

Gershunov, A., Shulgina, T., Ralph, F. M., Lavers, D. A., & Rutz, J. J. (2017). Assessing the climate-scale variability of atmospheric rivers affecting western North America. *Geophysical Research Letters*, *44*, 7900–7908.

Gill, A. E. (1982). Atmosphere-Ocean Dynamics. Academic Press, San Diego, 662 pp.

Gill, A. E., & Clarke, A. J. (1974). Wind-induced upwelling, coastal currents, and sea-level changes. *Deep-Sea Research*, *21*, 325–345.

Hendy, I. L., Napier, T. J., & Schimmelmann, A. (2015). From extreme rainfall to drought: 250 years of annually resolved sediment deposition in Santa Barbara Basin, California. *Quaternary International*, *387*, 3?12 (2015).

Hino, M., Belanger, S. T., Field, C. B., Davis, A. R., & Mach, K. J. (2019). High-tide flooding disrupts local economic activity. *Science Advances*, *5*, eaau2736.

392 Jevrejeva, S., Frederikse, T., Kopp, R. E., Le Cozannet, G., Jackson, L. P., & van de

393   Wal, R. S. W. (2019). Probabilistic Sea Level Projections at the Coast by 2100.

394   *Surveys in Geophysics*, *40*, 1673–1696.

395 Kalnay, E., Kanamitsu, M., Kistler, R., Collins, W., Deaven, D., Gandin, L., Iredell, M.,

396   Saha, S., White, G., Woollen, J., Zhu, Y., Chelliah, M., Ebisuzaki, W., Higgins, W.,

397   Janowiak, J., Mo, K. C., Ropelewski, C., Wang, J., Leetmaa, A., Reynolds, R. Jenne,

398   R., & Joseph, D. (1996). The NCEP/NCAR 40-year reanalysis project. *Bulletin of the*

399   *American Meteorological Society*, *77*, 3, 437–471.

400 Khouakhi, A., & Villarini, G. (2016). On the relationship between atmospheric rivers

401   and high sea water levels along the US West Coast. *Geophysical Research Letters*, *43*,

402   8815–8822.

403 Kriebel, D. L., & Geiman, J. D. (2013). A Coastal Flood Stage to Define Existing and

404   Future Sea-Level Hazards. *Journal of Coastal Research*, *30*, 5, 1017–1024.

405 Kopp, R. E., DeConto, R. M., Bader, D. A., Hay, C. C., Horton, R. M., Kulp, S.,

406   Oppenheimer, M., Pollard, M., & Strauss, B. H. (2017). Evolving Understanding of

407   Antarctic Ice-Sheet Physics and Ambiguity in Probabilistic Sea-Level Projections.

408   *Earth's Future*, *5*, 1217–1233.

409 Marcos, M., Calafat, F. M., Berihuete, A., & Dangendorf, S. (2015). Long-term

410   variations in global sea level extremes. *Journal of Geophysical Research: Oceans*, *120*,

411   8115–8134.

412 Menéndez, M., & Woodworth, P. L. (2010). Changes in extreme high water levels base

413   don a quasi-global tide-gauge data set. *Journal of Geophysical Research*, *115*, C1001.

Moftakhari, H. R., AghaKouchak, A., Sanders, B. F., & Matthew, R. A. (2017). Cumulative hazard: The case of nuisance flooding. *Earth's Future*, *5*, 214–223.

Moftakhari, H. R., AghaKouchak, A., Sanders, B. F., Allaire, M., & Matthew, R. A. (2018). What Is Nuisance Flooding? Defining and Monitoring an Emerging Challenge. *Water Resources Research*, *54*, 4218–4227.

Neiman, P. J., Ralph, F. M., Wick, G. A., Lundquist, J. D., & Dettinger, M. D. (2008). Meteorological characteristics and overland precipitation impacts of atmospheric rivers affecting the West Coast of North America based on eight years of SSM/I satellite observations. *Journal of Hydrometeorology*, *9*, 22–47.

Newman, M., Kiladis, G. N., Weickmann, K. M., Ralph, F. M., & Sardeshmukh, P. D. (2012). Relative contributions of synoptic and low-frequency eddies to time-mean atmospheric moisture transport, including the role of atmospheric rivers. *Journal of Climate*, *25*, 7341–7361.

Oakley, N. S., Lancaster, J. T., Kaplan, M. L., & Ralph, F. M. Synoptic conditions associated with cool season post-fire debris flows in the Transverse Ranges of southern California. *Natural Hazards*, *88*, 327–354.

Oakley, N. S., Lancaster, J. T., Hatchett, B. J., Stock, J., Ralph, F. M., Roj, S., & Lukashov, S. (2018). A 22-year climatology of cool season hourly precipitation thresholds conducive to shallow landslides in California. *Earth Interactions*, *22*, 1–35.

Payne, A. E., Demory, M.-E., Leung, L. R., Ramos, A. M., Shields, C. A., Rutz, J. J., Siler, N., Villarini, G., Hall, A., & Ralph, F. M. (2020). Responses and impacts of atmospheric rivers to climate change. *Nature Reviews Earth and Environment*, *1*,

143–157.

Pugh, D., & Woodworth, P. (2014). Sea-Level Science: Understanding Tides, Surges, Tsunamis, and Mean Sea-Level Changes. Cambridge University Press, Cambridge, 407 pp.

Ralph, F. M., Neiman, P. J., & Wick, G. A. (2004). Satellite and CALJET aircraft observations of atmospheric rivers over the eastern North Pacific Ocean during the winter of 1997/98. *Monthly Weather Review, 132*, 1721–1745.

Ralph, F. M., Coleman, T. A., Neiman, P. J., Zamora, R. J., & Dettinger, M. D. (2013) Observed impacts of duration and seasonality of atmospheric river landfalls on soil moisture and runoff in coastal Northern California. *Journal of Hydrometeorology, 14*, 443–459.

Ralph, F. M., Iacobellis, S. F., Neiman, P. J., Cordeira, J. M., Spackman, J. R., Waliser, D. E., Wick, G. A., White, A. B., & Fairall, C. (2017). Dropsonde observations of total integrated water vapor transport within North Pacific atmospheric rivers. *Journal of Hydrometeorology, 18*, 2577–2596.

Ray, R. D., & Merrifield, M. A. (2019). The Semiannual and 4.4-Year Modulations of Extreme High Tides. *Journal of Geophysical Research: Oceans, 124*, 5907–5922.

Ridder, N., de Vries, H., & Drijfhout, S. (2018). The role of atmospheric rivers in compound events consisting of heavy precipitation and high storm surges along the Dutch coast. *Natural Hazards and Earth System Sciences, 18*, 3311–3326.

Rutz, J. J., Shields, C. A., Lora, J. M., Payne, A. E., Guan, B., Ullrich, P., O'Brien, T., Leung, L. R., Ralph, F. M., Wehner, M., Brands, S., Collow, A., Goldenson, N.,

Gorodetskaya, I., Griffith, H., Kashinath, K., Kawzenuk, B., Krishnan, H., Kurlin, V.,
Lavers, D., Magnusdottir, G., Mahoney, K., McClenny, E., Muszynski, G., Nguyen, P.
D., Prabhat, M., Qian, Y., Ramos, A. M., Sarangi, C., Sellars, S., Shulgina, T., Tome,
R., Waliser, D., Walton, D., Wick, G., Wilson, A. M., & Viale, M. (2019). The
atmospheric river tracking method intercomparison project (ARTMIP): quantifying
uncertainties in atmospheric river climatology. *Journal of Geophysical Research:
Atmospheres*, *124*, 13777–13802.

Ryan, H. F., & Noble, M. A. (2006). Alongshore Wind Forcing of Coastal Sea Level as a
Function of Frequency. *Journal of Physical Oceanography*, *36*, 2173–2184.

Serafin, K. A., Ruggiero, P. & Stockdon, H. F. (2017). The relative contributions of
waves, tides, and nontidal residuals to extreme total water levels on U.S. West Coast
sandy beaches. *Geophysical Research Letters*, *44*, 1839–1847.

Shepherd, T. G. (2014). Atmospheric circulation as a source of uncertainty in climate
change projections. *Nature Geoscience*, *7*, 703–708.

Shields, C. A., Rutz, J. J., Leung, L-Y., Ralph, F. M., Wehner, M., Kawzenuk, B., Lora,
J. M., McClenny, E., Osborne, T., Payne, A. E., Ullrich, P., Gershunov, A.,
Goldenson, N., Guan, B., Qian, Y., Ramos, A. M., Sarangi, C., Sellars, S.,
Gorodetskaya, I., Kashinath, K., Kurlin, V., Mahoney, K., Muszynski, G., Pierce, R.,
Subramanian, A. C., Tome, R., Waliser, D., Walton, D., Wick, G., Wilson, A., Lavers,
D., Prabhat, M., Collow, A., Krishnan, H., Magnusdottir, G., & Nguyuen, P. (2018).
Atmospheric river tracking method intercomparison project (ARTMIP): project goals
and experimental design. *Geoscientific Model Development*, *11*, 2455–2474.

480 Shinoda, T., Zamudio, L., Guo, Y., Metzger, E. J., & Fairall, C. W. (2019). Ocean

481 variability and air-sea fluxes produced by atmospheric rivers. *Scientific Reports*, *9*,

482 2152.

483 Sweet, W. V., & Park, J. (2014). From the extreme to the mean: Acceleration and

484 tipping points of coastal inundation from sea level rise. *Earth's Future*, *2*, 579–600.

485 Sweet, W. V., Dusek, G., Obeysekera, O., & Marra, J. (2018). Patterns and Projections

486 of High Tide Flooding Along the U.S. Coastline Using a Common Impact Threshold.

487 NOAA Technical Report NOS CO-OPS 086, 56 pp.

488 Sweet, W. V., Simon, S. Dusek, G., Marcy, D., Brooks, W., Pendleton, M., & Marra, J.

489 (2021). 2021 State of High Tide Flooding and Annual Outlook. National Oceanic and

490 Atmospheric Administration, 28 pp.

491 Theuerkauf, E. J., Rodriguez, A. B., Fegley, S. R., & Luettich, R. A. (2014). Sea level

492 anomalies exacerbate beach erosion. *Geophysical Research Letters*, *41*, 5139–5147.

493 Thomson, R. E., & Emery, W. J. (2014). Data Analysis Methods in Physical

494 Oceanography, Third Edition. Elsevier, Waltham, 716 pp.

495 Thompson, P. R., Widlansky, M. J., Hamlington, B. D., Merrifield, M. A., Marra, J. J.

496 Mitchum, G. T., & Sweet, W. (2021). Rapid increases and extreme months in

497 projections of United States high-tide flooding. *Nature Climate Change*, *11*, 584–590.

498 Vallis, G. K., Zurita-Gotor, P., Cairns, C., & Kidston, J. (2015). Response of the

499 large-scale structure of the atmosphere to global warming. *Quarterly Journal of the*

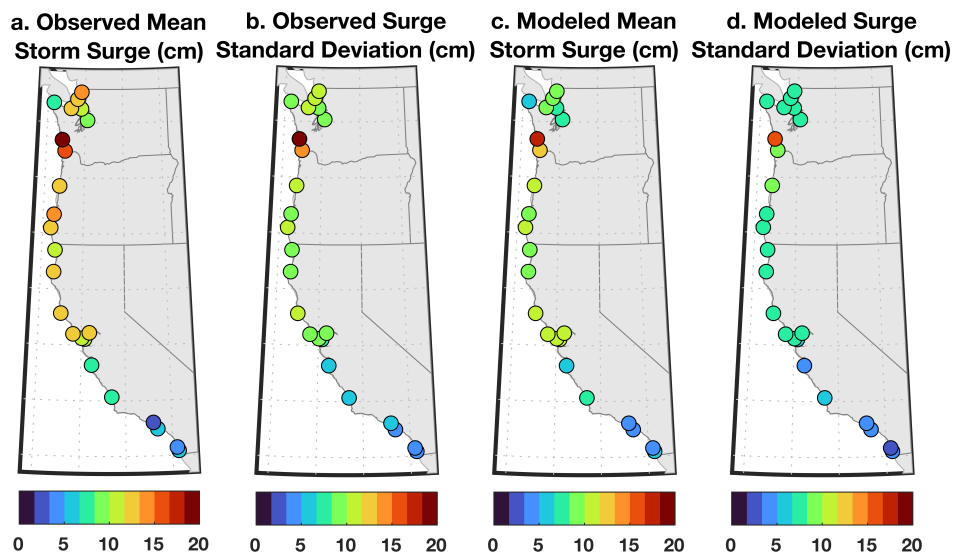500 *Royal Meteorological Society*, *141*, 1479–1501.

501   Verdy, A., Mazloff, M. R., Cornuelle, B. D., & Kim, S. Y. (2014). Wind-Driven Sea

502   Level Variability on the California Coast: An Adjoint Sensitivity Analysis. *Journal of*

503   *Physical Oceanography*, *44*, 297–318.

504   Wang, S. Y. S., Yoon, J.-H., Becker, E., & Gillies, R. (2017). California from drought to

505   deluge. *Nature Climate Change*, *7*, 465–468.

506   White, A. B., Moore, B. J., Gottas, D. J., & Neiman, P. J. (2019). Winter storm

507   conditions leading to excessive runoff above California?s Oroville Dam during January

508   and February 2017. *Bulletin of the American Meteorological Society*, *100*, 55–70.

509   Yin, J. H. (2005). A consistent poleward shift of the storm tracks in simulations of 21st

510   century climate. *Geophysical Research Letters*, *32*, L18701.

511   Zhu, Y., & Newell, R. E. (1998). A proposed algorithm for moisture fluxes from

512   atmospheric rivers. *Monthly Weather Review*, *126*, 725–735.
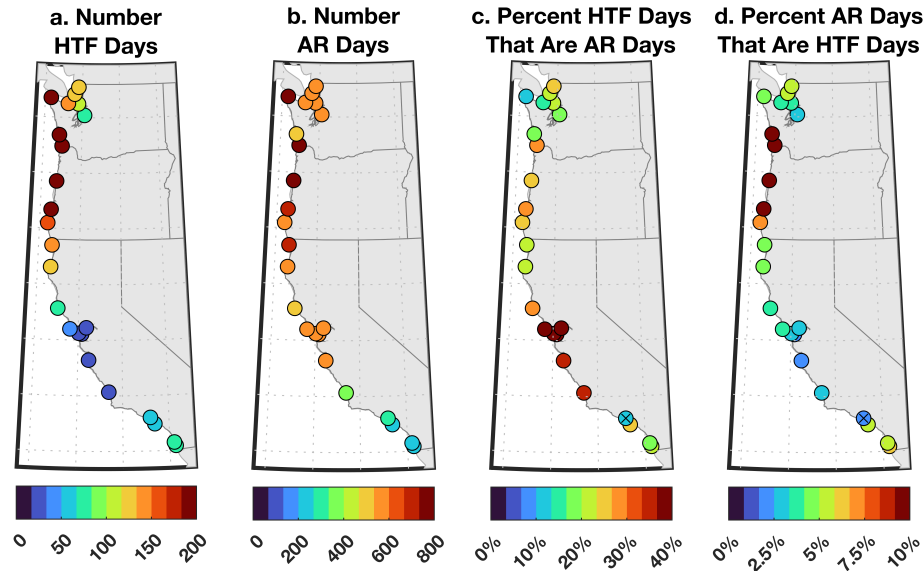
**Figure 1.** Number of **(a.)** HTF days and **(b.)** AR days at tide gauges during 1980–2016. Percentage of **(c.)** HTF days experiencing ARs, and **(d.)** AR days experiencing HTFs. The "x" at Santa Monica, California in panels (c.) and (d.) indicates that the value is not significant given the null hypothesis of two uncorrelated stochastic Poisson processes (Supporting Information Text S2).
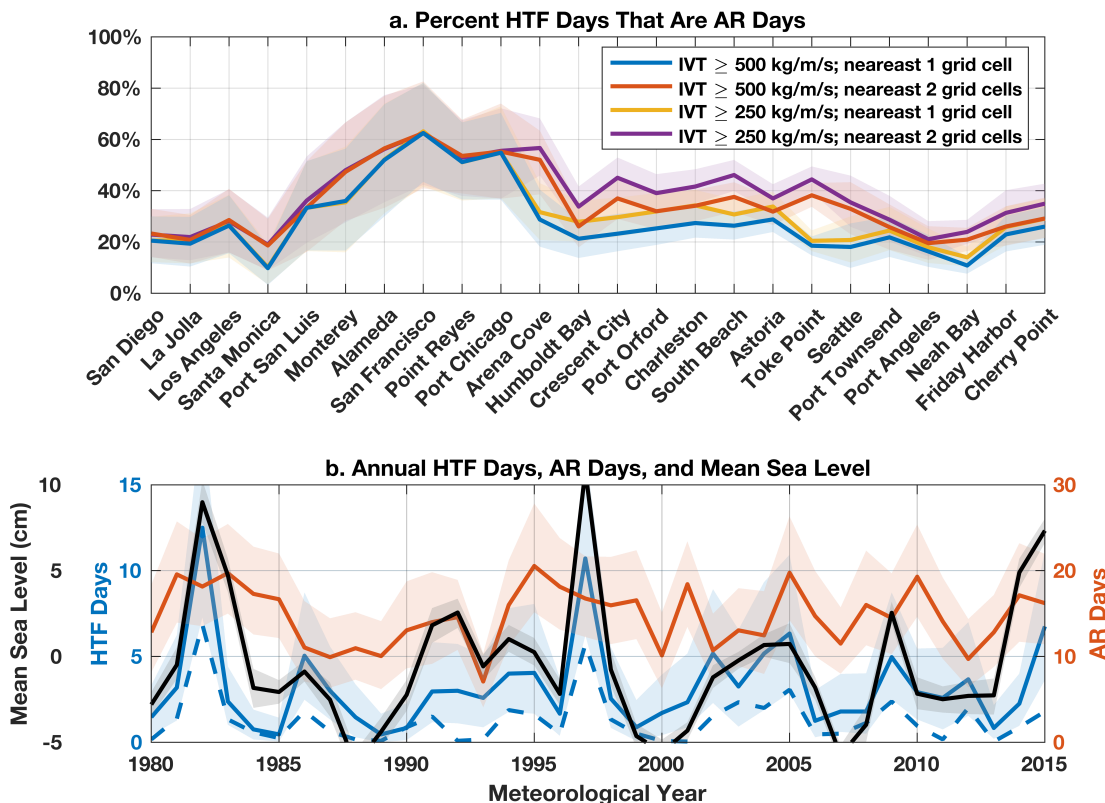
Figure 2. **(a.)** Percentage of HTF days with ARs during 1980–2016. Different colors identify different criteria applied to determine whether an AR is nearby during a HTF (i.e., whether the minimum IVT threshold is 250 or 500 kg m^{-1} s^{-1} and 1 or 2 nearby grid cells are considered). **(b.)** Averages across all tide gauges along the US West Coast of yearly observed HTF days (blue), AR days (orange), and annual mean sea level (black). Thick lines and shaded values are, respectively, bootstrap estimates of average values and 95% confidence intervals. Blue dashed line is the best estimate of the number of HTF days per year expected hypothetically from tides and mean sea-level changes (see text for details). Note that the horizontal axis has units of meteorological years (April–May).

a. Observed Mean Storm Surge (cm)   **b. Observed Surge Standard Deviation (cm)**   **c. Modeled Mean Storm Surge (cm)**   **d. Modeled Surge Standard Deviation (cm)**

Figure 3. Composite **(a.)** averages and **(b.)** standard deviations of storm surge during ARs observed by tide gauges over 1980–2016. **(c.), (d.)** As in (a.), (b.) but based on the ridge-regression model including local wind, pressure, and precipitation forcing.
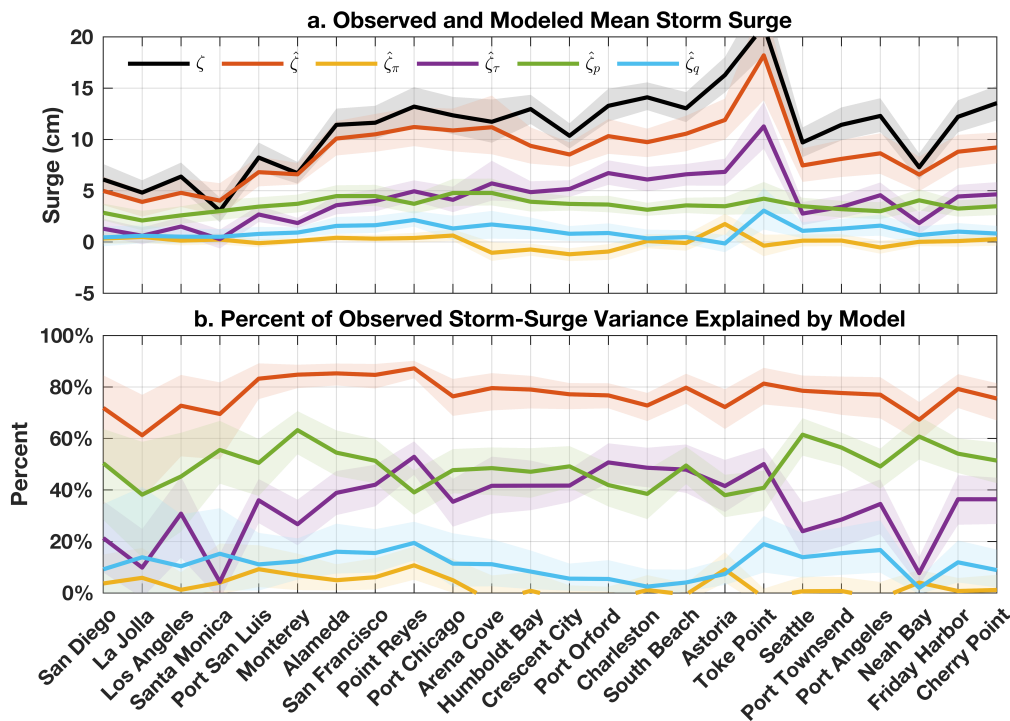
Figure 4. **(a.)** Average ζ value across all ARs observed by tide gauges during 1980–2016 (black) alongside corresponding total $\hat{\zeta}$ (orange), zonal-wind-driven $\hat{\zeta}_\pi$ (yellow), meridional-wind-driven $\hat{\zeta}_\tau$ (purple), pressure-driven $\hat{\zeta}_p$ (green), precipitation-driven $\hat{\zeta}_q$ (blue) modeled values. **(b.)** Observed ζ variance explained by the various model estimates at each tide gauge during 1980–2016. Thick lines and shaded values are, respectively, bootstrap estimates of the mean and 95% confidence interval. We define the variance V in a variable x explained by another variable y as $V = 100\% \times \left[1 - \mathrm{var}\left(x - y\right)/\mathrm{var}\left(x\right)\right]$ where var is the variance operator.

₁ Supporting Information for "High-Tide Floods and ₂ Storm Surges During Atmospheric Rivers on the US ₃ West Coast"

Christopher G. Piecuch[1], Sloan Coats[2], Sönke Dangendorf[3], Felix W.

Landerer[4], J. T. Reager[4], Philip R. Thompson[2], and Thomas Wahl[5]

—————

Christopher G. Piecuch, Woods Hole Oceanographic Institution, 266 Woods Hole Road, Woods

Hole, MA 02543, USA. (cpiecuch@whoi.edu)

[1]Woods Hole Oceanographic Institution,

Woods Hole, MA, USA.

[2]University of Hawai'i at Mānoa,

Honolulu, HI, USA.

[3]Old Dominion University, Norfolk, VA,

USA

[4]Jet Propulsion Laboratory, Pasadena,

CA, USA.

[5]University of Central Florida, Orlando,

FL, USA.

D R A F T   August 24, 2021, 9:27am   D R A F T

S1. Bootstrapping

⁴ We use bootstrapping to quantify uncertainty related to the finite record lengths of

⁵ the data (e.g., Efron and Hastie, 2016). Given time-series data (e.g., hourly tide-gauge

⁶ water-level observations), for each sample statistic (e.g., mean, standard deviation), we

⁷ perform 1,000 iterations of randomly selecting (with replacement) a number of data

⁸ values equal to the length of the original data record and computing the sample

⁹ statistic. Since values can be repeated or omitted, statistics computed during any given

¹⁰ iteration can differ from the value computed from the original data. Values in the main

¹¹ text are usually given in the form of averages or 95% confidence intervals from the

¹² resulting distributions.

¹³ Note that, for quantities that depend on the covariance between time series (e.g.,

¹⁴ variance explained, co-occurrence of HTFs and ARs), we randomly select the time

¹⁵ points at each bootstrapping iteration and use those common time points for each data

¹⁶ series involved in the calculation. For example, we compute regression coefficients using

¹⁷ contemporaneous storm surge, wind stress, barometric pressure, and freshwater flux.

¹⁸ A caveat of the bootstrapping method used here is that it is performed independently

¹⁹ at each tide-gauge location. Thus, when computing spatial averages, we will tend to

²⁰ underestimate the true uncertainties, since the approach effectively assumes that errors

²¹ are uncorrelated across tide gauges. In reality, there are spatial dependencies in the

²² processes under consideration that should be taken into account in a more complete

²³ future spatiotemporal statistical analysis.

S2. Hypothesis testing

To evaluate whether relationships between quantities of interest in section 3 of the main text are statistically significant, we run Monte Carlo simulations of synthetic stochastic processes. For example, we compute the significance of the co-occurrence of (or correlation between) HTFs and ARs by comparing observed values (Figures 1, 2) to values expected from two independent stochastic daily Poisson processes with parameter values determined from the observed numbers of HTF days and AR days during the study period. The corresponding P-value is calculated as the fraction of the time that co-occurrences are more frequent (or that correlations are stronger) in the simulations than in the observations. Likewise, we quantify the significance of the correlation between interannual time series of HTFs and mean sea level (Figure 2b) by comparing to simulated correlations between a random Poisson process with parameter value based on the observed number of HTFs and a random zero-mean Gaussian process with variance parameter equal to the variance of the observed mean sea-level time series.

S3. Ridge regression

Consider the linear model

$$\mathbf{y} = \mathbf{X}\beta + \epsilon \tag{S1}$$

where $\mathbf{y}$ is the $n \times 1$ known observational vector, $\mathbf{X}$ is the $n \times p$ known structure matrix, ϵ is the $n \times 1$ noise vector, and β is the $p \times 1$ vector of unknown parameters to be determined. With reference to Eq. (1) in the main text, the vector $\mathbf{y}$ in Eq. (S1) corresponds to the observed storm surge, matrix $\mathbf{X}$ corresponds to the local wind, pressure, and precipitation forcing, and vector β corresponds to the a and b terms.

The ordinary least squares estimate of the parameter vector is

$$\hat{\beta}_{\mathrm{OLS}} = \left(\mathbf{X}^{\mathsf{T}}\mathbf{X}\right)^{-1}\mathbf{X}^{\mathsf{T}}\mathbf{y}. \tag{S2}$$

[42] If elements of the structure matrix are collinear, then the inner product matrix $\mathbf{X}^{\mathsf{T}}\mathbf{X}$

[43] can be poorly conditioned (or even singular), resulting in large uncertainties on $\hat{\beta}_{\mathrm{OLS}}$.

[44] This is a concern in the present context, since the predictor variables can be correlated.

[45] As just one randomly selected example, the Pearson correlation coefficient between

[46] anomalous meridional wind stress and barometric pressure across 108 landfalling ARs at

[47] Port Chicago, California during 1980–2016 is -0.53 ($P < 0.01$).

Ridge regression is a regularization technique that gives more accurate (but biased)

estimates relative to ordinary least squares in problems with correlated predictors. The

ridge-regression estimate of the parameter vector is (e.g., Efron and Hastie, 2016)

$$\hat{\beta}_{\mathrm{RR}} = \left(\mathbf{X}^{\mathsf{T}}\mathbf{X} + \lambda\mathsf{I}\right)^{-1}\mathbf{X}^{\mathsf{T}}\mathbf{y}. \tag{S3}$$

[48] where $\lambda > 0$ is a real constant and I is the identity matrix. See Efron and Hastie (2016)

[49] for a Bayesian interpretation of λ in terms of prior belief.

[50] We use Eq. (S3) with $\lambda = 0.3$ to solve for the a's and b's in Eq. (1) in the main text.

[51] Results are robust to the selection of λ, and similar regression coefficients are found for a

[52] wide range of λ values (Figure S3). Before evaluating Eq. (S3), we standardize the

[53] predictors to have zero mean and unit sum of squares. We also remove the mean from

[54] the observational vector. After computing $\hat{\beta}_{\mathrm{RR}}$, we rescale the regression coefficients

[55] back to their respective physical units (cf. Figure S3).

S4. Theoretical coefficients

To interpret regression coefficients determined empirically from the data (Figure S3), we build a model of the coastal sea-level response to surface wind, pressure, and precipitation forcing. Imagine a straight coastline extending infinitely in the meridional/alongshore (y) coordinate. The coast faces the ocean to the west, with the origin in the zonal/onshore coordinate (x) at the coast. Offshore positions have values $x < 0$. We consider the following form of shallow water equations

$$\eta_t + H u_x = 0, \tag{S4}$$

$$-fv = -g \left[\eta + \frac{1}{\rho g} p + \int^t q(t') \, dt' \right]_x + \frac{1}{\rho H} \pi, \tag{S5}$$

$$v_t + fu = \frac{1}{\rho H} \tau - \gamma v. \tag{S6}$$

Here t is time, subscript is partial differentiation, p is barometric pressure, q is precipitation, π and τ are onshore and alongshore wind stress, respectively, η is adjusted sea level (Gill, 1982; Ponte, 2006)

$$\eta \doteq \zeta - \int^t q(t') \, dt', \tag{S7}$$

where ζ is sea level, u is onshore velocity, v is alongshore velocity, ρ is constant ocean density, g is gravitational acceleration, f is the Coriolis parameter, H is constant ocean depth, and $\gamma \doteq r/H$ is an inverse timescale, where r is a linear friction coefficient.

The choice of the locally forced form of Eqs. (S4)–(S6) is partly motivated by the regression analysis, which suggests that observed storm surges can be largely understood in terms of local wind, pressure, and precipitation forcing (Figure 4). We have omitted terms involving the onshore velocity in the onshore momentum equation, and the effects

63 of stratification, nonlinearities, and alongshore dependence in the governing equations.

64 These omissions follow formally from the assumptions that Burger and Rossby numbers

65 are small, alongshore scales are much larger than onshore scales, alongshore motions are

66 much stronger than onshore motions, and frequencies are sub-inertial.

We suppose that surface forcing by an AR is described by temporal plane waves that
decay spatially away from the coast

$$F(x,t) = F_0 \exp(kx - i\sigma t), \ F \in \{p, q, \pi, \tau\}, \tag{S8}$$

where $i \doteq \sqrt{-1}$, σ is angular frequency, and k and F_0 are real constants. We demand
that the oceanic response is separable and described by plane waves in time

$$y(x,t) = \tilde{y}(x) \exp(-i\sigma t), \ y \in \{\eta, u, v\}, \tag{S9}$$

67 where $\tilde{\eta}$, $\tilde{u}$, and $\tilde{v}$ are functions of the onshore coordinate to be determined.

Inserting (S8) and (S9) into (S4)–(S6) and rearranging gives a second-order
inhomogeneous linear ordinary differential equation for onshore structure

$$\tilde{\eta}_{xx} - \kappa^2 \tilde{\eta} = \left[-\frac{k}{\rho g} p_0 - i\frac{k}{\sigma} q_0 + \frac{1}{\rho g H} \pi_0 + \frac{f}{\rho g H} \left(\frac{\gamma + i\sigma}{\gamma^2 + \sigma^2} \right) \tau_0 \right] k \exp(kx) \tag{S10}$$

68 where $\kappa \doteq s \exp(i\varphi)/L_R$ is complex, with barotropic Rossby radius of deformation

69 $L_R \doteq \sqrt{gH}/f$, amplitude $s \doteq \left[1 + (\gamma/\sigma)^2 \right]^{-1/4}$, and phase $\varphi \doteq \frac{1}{2} \arctan(-\gamma/\sigma)$.

The boundary conditions are

$$\eta \to 0 \text{ as } x \to -\infty, \tag{S11}$$

$$\tilde{\eta}_x = -\frac{k}{\rho g} p_0 - i\frac{k}{\sigma} q_0 + \frac{1}{\rho g H} \pi_0 + \frac{f}{\rho g H} \left(\frac{\gamma + i\sigma}{\gamma^2 + \sigma^2} \right) \tau_0 \text{ at } x = 0. \tag{S12}$$

70 The first boundary condition demands a shore-trapped solution, whereas the second

71 boundary condition can be shown to be a form of no-normal flow through the boundary.

The solution to Eq. (S10) subject to Eqs. (S11) and (S12) is

$$\tilde{\eta}(x) = \frac{k\exp(kx) + \kappa\exp(-\kappa x)}{k^2 - \kappa^2}\left[-\frac{k}{\rho g}p_0 - i\frac{k}{\sigma}q_0 + \frac{1}{\rho g H}\pi_0 + \frac{f}{\rho g H}\left(\frac{\gamma + i\sigma}{\gamma^2 + \sigma^2}\right)\tau_0\right].$$

(S13)

which, at the coast, simplifies to

$$\tilde{\eta}(x=0) = \frac{1}{k-\kappa}\left[-\frac{k}{\rho g}p_0 - i\frac{k}{\sigma}q_0 + \frac{1}{\rho g H}\pi_0 + \frac{f}{\rho g H}\left(\frac{\gamma + i\sigma}{\gamma^2 + \sigma^2}\right)\tau_0\right]. \quad (S14)$$

Adding iq_0/σ to convert from effective sea level to sea level [cf. Eq. (S7)] and scaling by $\exp(-i\sigma t)$, we obtain the time-variable coastal sea-level solution

$$\zeta(x=0,t) = \frac{1}{k-\kappa}\left[-\frac{k}{\rho g}p - i\frac{\kappa}{\sigma}q + \frac{1}{\rho g H}\pi + \frac{f}{\rho g H}\left(\frac{\gamma + i\sigma}{\gamma^2 + \sigma^2}\right)\tau\right], \quad (S15)$$

where, on the right side, we understand the forcing terms to be evaluated at the coast.

Recognizing that $i\exp(-i\sigma t) = \mathcal{H}[\exp(-i\sigma t)]$ by definition of the Hilbert transform $\mathcal{H}$, and in analogy with Eq. (1) in the main text, we can write Eq. (S15) equivalently as

$$\zeta(x=0,t) = a_\pi\pi + b_\pi\mathcal{H}(\pi) + a_\tau\tau + b_\tau\mathcal{H}(\tau) + a_p p + b_p\mathcal{H}(p) + a_q q + b_q\mathcal{H}(q), \quad (S16)$$

where

$$a_\pi \doteq \Re\left[\frac{1}{k-\kappa}\left(\frac{1}{\rho g H}\right)\right], \quad b_\pi \doteq \Im\left[\frac{1}{k-\kappa}\left(\frac{1}{\rho g H}\right)\right], \quad (S17)$$

$$a_\tau \doteq \Re\left\{\frac{1}{k-\kappa}\left[\frac{f}{\rho g H}\left(\frac{\gamma+i\sigma}{\gamma^2+\sigma^2}\right)\right]\right\}, \quad b_\tau \doteq \Im\left\{\frac{1}{k-\kappa}\left[\frac{f}{\rho g H}\left(\frac{\gamma+i\sigma}{\gamma^2+\sigma^2}\right)\right]\right\}, \quad (S18)$$

$$a_p \doteq \Re\left[\frac{1}{k-\kappa}\left(-\frac{k}{\rho g}\right)\right], \quad b_p \doteq \Im\left[\frac{1}{k-\kappa}\left(-\frac{k}{\rho g}\right)\right], \quad (S19)$$

$$a_q \doteq \Re\left[\frac{1}{k-\kappa}\left(-i\frac{\kappa}{\sigma}\right)\right], \quad b_q \doteq \Im\left[\frac{1}{k-\kappa}\left(-i\frac{\kappa}{\sigma}\right)\right], \quad (S20)$$

and where $\Re$ and $\Im$ correspond to real and imaginary parts, respectively.

To evaluate Eqs. (S17)–(S20), we use reasonable, representative numerical values or ranges for the various parameters (Table S2). We assume that σ is between $2\pi/(1\text{ day})$

76 and $2\pi / (6 \text{ days})$. This range is selected because roughly two-thirds of the landfalling

77 ARs considered here have lifetimes between 1 and 6 days (not shown).

78   In Figure S3, we compare numerical values of the various a and b terms determined

79 empirically from ridge regression applied to the data to those values expected

80 theoretically from first principles as embodied in Eqs. (S17)–(S20) and evaluated as

81 described in the previous paragraph. Empirical values are shown as a function of

82 ridge-regression parameter λ and represent 95% confidence intervals across all tide

83 gauges and bootstrap iterations. Theoretical values are shown as minima and maxima

84 based on the parameter values in Table S2 and the target frequency range.

85   Acknowledging that uncertainties are large, we find that empirical and theoretical

86 coefficients are roughly consistent to order of magnitude, overlapping within their

87 estimated uncertainties (Figure S3). This supports the hypothesis that statistical results

88 in the main text are informative of causal relationships. Note that, in mentioning the

89 rough consistency between empirical and theoretical results, we are not arguing that the

90 analytical model represents all of the relevant physics underlying ζ during ARs. This

91 model framework is highly simplified, and omits many factors that may be important in

92 the real world (e.g., stratification, nonlinearities, alongshore dependence, topographic

93 variation). Our goal here was to identify a simple model based on reasonable

94 assumptions and amenable to analytical solution to show that statistical relationships

95 between forcing and response obtained through regression analysis are not in gross

96 conflict with expectations from basic physics. While we believe we have largely

97 accomplished this goal, we recognize that our results identify open questions. For

98 example, while the estimates feature overlapping uncertainties, empirical values of a_π are

99 largely negative, whereas first principles predict a positive a_π value (Figure S3 top left).

100 (Keep in mind that, according to regression analysis, π is not an important ζ driver.)

101 We speculate that this discrepancy could reflect unphysical relationships inferred by the

102 regression analysis or important physics not represented in the analytical model. Future

103 studies based on more comprehensive causal frameworks (e.g., high-resolution general

104 circulation models) could revisit these questions to identify more unambiguously the

105 relative roles of different forcing mechanisms and the nature of the oceanic response.

References

106 Efron, B., & Hastie, T. (2016). Computer Age Statistical Inference: Algorithms, Evidence, and

107   Data Science. Cambridge University Press, Cambridge, 475 pp.

108 Gill, A. E. (1982). Atmosphere-Ocean Dynamics. Academic Press, San Diego, 662 pp.

109 Ponte, R. M. (2006). Oceanic Response to Surface Loading Effects Neglected in

110   Volume-Conserving Models. *Journal of Physical Oceanography, 36*, 426–434,

111   https://doi.org/10.1175/JPO2843.1.

| Station	ID	Latitude	Longitude	Completeness	Threshold (cm)	99.5th Percentile (cm)
San Diego	9410170	32.7°N	117.2°W	99.2%	57.0	37.8
La Jolla	9410230	32.9°N	117.3°W	99.7%	56.5	36.3
Los Angeles	9410660	33.7°N	118.3°W	100.0%	56.7	36.0
Santa Monica	9410840	34°N	118.5°W	91.4%	56.6	37.0
Port San Luis	9412110	35.2°N	120.8°W	99.5%	56.5	32.4
Monterey	9413450	36.6°N	121.9°W	99.7%	56.5	31.7
Alameda	9414750	37.8°N	122.3°W	99.8%	58.0	27.4
San Francisco	9414290	37.8°N	122.5°W	99.8%	57.1	28.1
Point Reyes	9415020	38.0°N	123.0°W	98.9%	57.0	32.5
Port Chicago	9415144	38.1°N	122.0°W	98.5%	56.0	26.9
Arena Cove	9416841	38.9°N	123.7°W	78.8%	57.2	34.8
Humboldt Bay	9418767	40.8°N	124.2°W	98.4%	58.4	37.7
Crescent City	9419750	41.7°N	124.2°W	98.8%	58.4	36.0
Port Orford	9431647	42.7°N	124.5°W	87.2%	58.9	39.3
Charleston	9432780	43.3°N	124.3°W	98.5%	59.3	40.5
South Beach	9435380	44.6°N	124.0°W	99.3%	60.2	43.3
Astoria	9439040	46.2°N	123.8°W	99.3%	60.5	44.4
Toke Point	9440910	46.7°N	124.0°W	92.2%	60.9	51.1
Seattle	9447130	47.6°N	122.3°W	100.0%	63.8	34.9
Port Townsend	9444900	48.1°N	122.8°W	99.6%	60.4	36.3
Port Angeles	9444090	48.1°N	123.4°W	98.8%	58.6	41.5
Neah Bay	9443090	48.4°N	124.6°W	99.7%	59.7	46.0
Friday Harbor	9449880	48.5°N	123.0°W	99.9%	59.5	39.1
Cherry Point	9449424	48.9°N	122.8°W	98.5%	61.2	37.2

112 **Table S1.** Name, identification number, latitude, longitude, completeness, HTF threshold, and

113 99.5th percentile of tide-gauge stations and their hourly still water level records during

114 1980–2016. Identification numbers are as provided by NOAA. Completeness refers to the

115 percentage of hours during the study period for which the tide gauge returned valid hourly still

116 water level data. HTF threshold is a linear function of great diurnal range (difference between

117 mean higher high water and mean lower low water) after Sweet et al. (2018). Values for HTF

118 threshold and 99.5th percentile are relative to mean higher high water. Note that the

119 Humboldt Bay tide gauge is also known as North Spit.

| Parameter	Description	Value
ζ	Sea Level	—
η	Effective Sea Level	—
u	Onshore Velocity	—
v	Alongshore Velocity	—
τ	Meridional Wind Stress	—
π	Zonal Wind Stress	—
q	Precipitation	—
p	Barometric Pressure	—
t	Time	—
x	Onshore Coordinate	—
σ	Angular Frequency	—
ρ	Ocean Density	1000 kg m^{-3}
g	Gravitational Acceleration	10 m s^{-2}
k	Offshore Decay Scale	50–200 km
H	Shelf Depth	100–200 m
f	Coriolis Parameter	0.6–1.1×10^{-4} s^{-1}
r	Friction Coefficient	1×10^{-4}–1×10^{-2} m s^{-1}
γ	Inverse Frictional Timescale	5×10^{-7}–1×10^{-4} s^{-1}

Table S2. Analytical model variables and parameters. Reasonable parameter values and ranges are given where applicable.
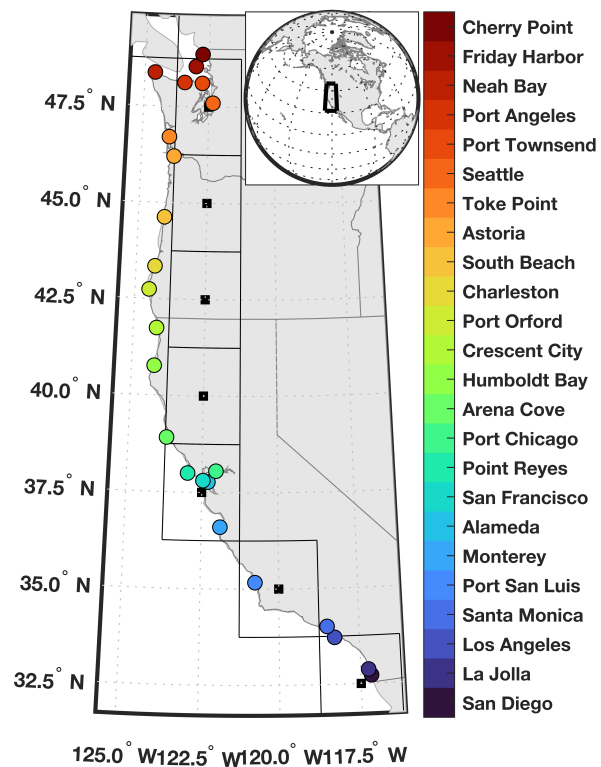
Figure S1. Study region. Colored circles identify locations of tide gauges. Thick black squares

mark centers of grid cells in the catalog of ARs. Thin square outlines denote $2.5° \times 2.5°$ catalog

grid-cell boundaries. Inset shows study region in global context.
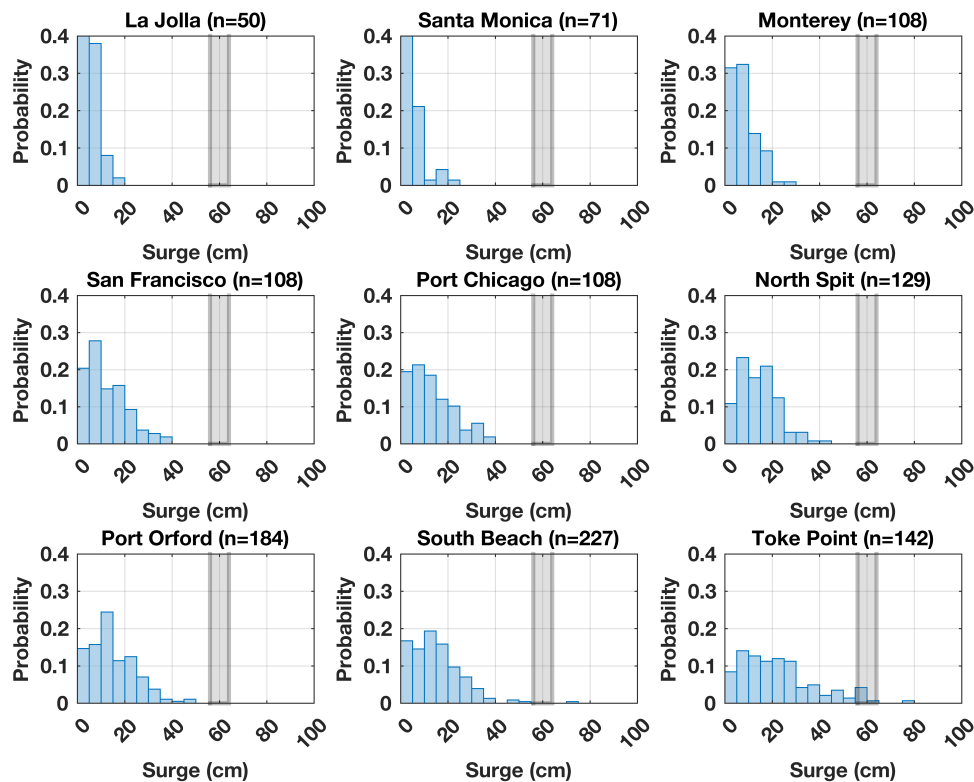
Figure S2. Blue shading shows probability density functions of surges during ARs at example tide gauges (location names and number of AR events identified in the title of each panel). For reference, gray shading identifies the 56–64-cm range that encompasses the HTF thresholds (above mean higher high water) at the tide gauges (cf. Table S1).
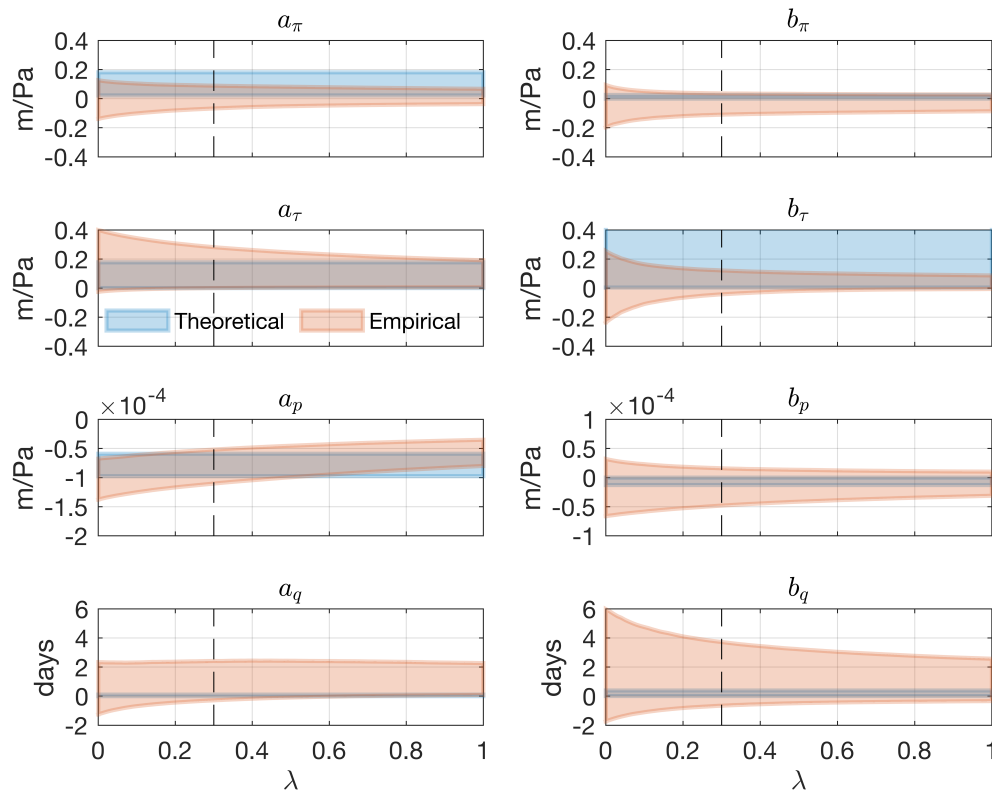
Figure S3. Coefficients between atmospheric forcing and storm surge ζ found empirically from regression analysis (orange) and expected theoretically from the analytical model (blue). Left column shows coefficients between ζ and atmospheric forcing [a's in Eqs. (1), (S16)–(S20)], whereas right column shows coefficients between ζ and the Hilbert transforms of atmospheric forcing [b's in Eqs. (1), (S16)–(S20)]. First row shows results for zonal wind stress π, second row meridional wind stress τ, third row barometric pressure p, and fourth row precipitation q. Empirical values are 95% confidence intervals across all sites as a function of ridge-regression parameter λ (vertical black dashes identify $\lambda = 0.3$). Theoretical values are shown as min/max ranges based on Eqs. (S16)–(S20) evaluated using parameter values/ranges in Table S2 and an angular frequency σ range between $2\pi/(1\text{ day})$ and $2\pi/(6\text{ days})$.